

The nature of HHL 73 from optical imaging and Integral Field Spectroscopy

R. López,^{1*} S. F. Sánchez,^{2*} B. García-Lorenzo,^{3*} G. Gómez,^{3,4*}
R. Estalella,^{1*} A. Riera^{5*} and G. Busquet^{1*} †

¹Departament d'Astronomia i Meteorologia, Universitat de Barcelona, Martí i Franquès 1, E-08028 Barcelona, Spain.

²Centro Astronómico Hispano-Alemán de Calar Alto, Jesús Durban Remon 2-2, E-04004 Almería, Spain.

³Instituto de Astrofísica de Canarias, E-38200 La Laguna, Spain

⁴GTC Project Office, GRANTECAN S.A. (CALP), E-38712 Breña Baja, La Palma, Spain.

⁵Dept. Física i Enginyeria Nuclear. EUETI de Barcelona. Universitat Politècnica de Catalunya. Compte d'Urgell 187, E-08036 Barcelona, Spain.

Accepted. Received;

ABSTRACT

We present new results on the nature of the Herbig–Haro-like object 73 (HHL 73, also known as [G84b] 11) based on narrow-band CCD $H\alpha$ and [S II] images of the HHL 73 field, and Integral Field Spectroscopy and radio continuum observations at 3.6 cm covering the emission of the HHL 73 object. The CCD images allow us to resolve the HHL 73 comet-shaped morphology into two components and a collimated emission feature of ~ 4 -arcsec long, reminiscent of a microjet. The IFS spectra of HHL 73 showed emission lines characteristic of the spectra of Herbig–Haro objects. The kinematics derived for HHL 73 are complex. The profiles of the [S II] $\lambda\lambda 6717, 6731$ Å lines were well fitted with a model of three Gaussian velocity components peaking at $V_{\text{LSR}} \simeq -100, -20$ and $+35$ km s⁻¹. We found differences among the spatial distribution of the kinematic components that are compatible with the emission from a bipolar outflow with two blueshifted (low- and high-velocity) components. Extended radio continuum emission at 3.6 cm was detected showing a distribution in close agreement with the HHL 73 redshifted gas. From the results discussed here, we propose HHL 73 to be a true HH object. *IRAS* 21432+4719, offset 30 arcsec northeast from the HHL 73 apex, is the most plausible candidate to be driving HHL 73, although the evidence is not conclusive.

Key words: ISM: jets and outflows – ISM: individual: [G84b] 11, HHL 73, HH 379, *IRAS* 21432+4719

1 INTRODUCTION

Herbig–Haro-like objects (HHLs) appear as bright nebulosities in the red optical images. Spectroscopy of HHLs indicates that a fraction of them are reflection nebulae originated by the scattered light from a stellar source associated with the nebulosity, while only a fraction of HHLs are Herbig–Haro (HH) objects arising from shock-excited gas. HHL 73, also known as [G84b] 11, was first reported by Gyulbudaghian (1984) as object 11 found in his survey of *DSS* red plates. In these plates, the object shows a comet-shaped morphology, being located close to the western border of

a region with high visual extinction. In fact, HHL 73 is found associated with a dark cloud complex in Cygnus, close to the Lynds Dark Cloud 1035A (*LDN* 1035A), and lying in a region with clear signs of recent star formation activity. The estimated distance to the region is 900 ± 100 pc (Elias 1978).

The source *IRAS* 21432+4719 is located close to HHL 73. Both sources are engulfed within a clump of high-density molecular gas, traced by the emission of the NH_3 and CS molecules, whose emission peaks around the HHL 73 and *IRAS* 21432+4719 positions (see Anglada, Sepúlveda & Gómez 1997 and references therein for a wider description on the high-density molecular gas emissions in the HHL 73 field). Emission from high-velocity molecular gas in this field is also reported by Dobashi et al. (1993), who detect a highly asymmetric CO bipolar outflow. The emission of the redshifted outflow lobe is spatially more extended than the blueshifted lobe and encompasses the region around *IRAS* and HHL 73. In addition, the detection of a water maser near HHL 73 was reported by Gyulbudaghian, Rodríguez & Mendoza-Torres (1987).

Devine, Reipurth & Bally (1997) imaged the HHL 73 field

* E-mail: rosario@am.ub.es; sanchez@caha.es; bgarcia@iac.es; gabriel.gomez@gtc.iac.es; robert.estalella@am.ub.es; angels.riera@upc.edu; gbusquet@am.ub.es

† Based on observations collected at the Centro Astronómico Hispano Alemán (CAHA) at Calar Alto, operated jointly by the Max-Planck Institut für Astronomie and the Instituto de Astrofísica de Andalucía (CSIC) and in the 2.6 m Nordic Optical Telescope and 2.5 m Isaac Newton Telescope at the Observatorio del Roque de los Muchachos of the Instituto de Astrofísica de Canarias.

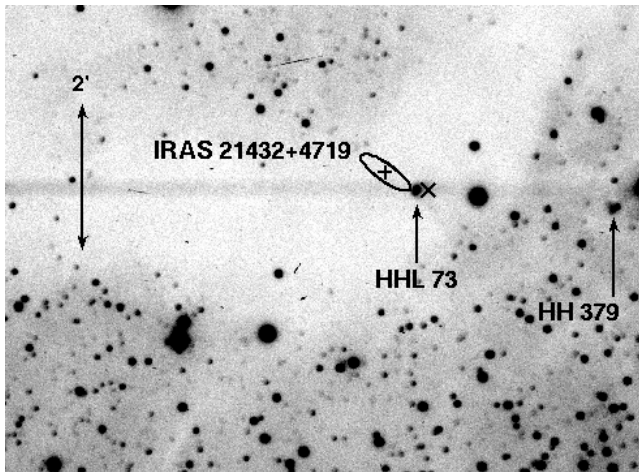


Figure 1. CCD $H\alpha$ -band image of the HHL 73 field obtained at the Isaac Newton Telescope (INT, ORM). Arrows point to the HHL 73 and HH 379 objects. The position of *IRAS* 21432+4719 and the error ellipse are marked. The tilted cross marks the position given by Gyulbudaghian, Rodríguez & Mendoza-Torres (1987) for the H_2O maser. The image FOV is $\sim 8.5 \times 6$ arcmin². North is up and east is to the left.

through narrow-band $H\alpha$ and $[S\ II] \lambda\lambda 6717, 6731$ Å filters. They find two stellar-like condensations ~ 2.5 arcmin west of HHL 73 with similar $H\alpha$ and $[S\ II]$ surface brightness, surrounded by diffuse emission. They designate their finding as the new Herbig–Haro object HH 379. In addition, they suggest that the exciting source of HH 379 may be embedded within the cometary nebula which appears in their images at a position close to *IRAS* 21432+4719 (thus, at the position given by Gyulbudaghian (1984) for HHL 73). These authors also discuss a plausible association between the *IRAS* source and the undetected exciting source of HH 379. It should be noted that Devine, Reipurth & Bally (1997) never refer to the optical cometary nebula as the HHL 73 object reported by Gyulbudaghian (1984). Later on, Davis et al. (2001, 2003) performed near-*IR* echelle spectroscopy at the HHL 73 position. They detect emission from $H_2 \lambda 2.122$ μm and $[\text{Fe}\ II] \lambda 1.644$ μm lines, while no continuum emission is detected at the HHL 73 position. Both lines show a rather complex profile, the width of the $[\text{Fe}\ II]$ line being roughly twice that of the H_2 line. Davis et al. (2003) suggest that the $[\text{Fe}\ II]$ emission may trace the higher-velocity component of a jet. In addition, Davis et al. (2001, 2003) also suggest that the optical nebula found in the Devine, Reipurth & Bally (1997) images harbours the true exciting source of HH 379, thus discarding the possibility that *IRAS* 21432+4719 was driving HH 379. This yet undetected exciting source of HH 379 is named as HH 379-IRS by these authors. In order to help with the identification of the sources mentioned here, we show in Fig. 1 a CCD $H\alpha$ image of the HHL 73 field where all these sources have been marked.

With the aim of unravelling the nature of HHL 73, we included this target within a programme of Integral Field Spectroscopy (IFS) of Herbig–Haro objects using the Potsdam Multi-Aperture Spectrophotometer (PMAS) in the wide-field IFU mode PPAK. Additional CCD narrow-band images and radio continuum 3.6 cm data have been analysed to complement the study. We present in this paper the results on the kinematics and physical conditions of HHL 73 obtained from this IFS pilot programme.

The paper is organized as follows. The observations and data reduction of CCD imaging, radio continuum and IFS observations are described in § 2.1, 2.2 and 2.3 respectively. Results are given in

§ 3: CCD imaging in § 3.1, radio continuum in § 3.2 and IFS in § 3.3, including results from integrated emission (§ 3.4) and a line-profile decomposition model for $[S\ II]$ profiles (§ 3.5). A global discussion is made in § 4. In § 5 the main conclusions are summarized.

2 OBSERVATIONS AND DATA REDUCTION

2.1 Narrow-band CCD images

Narrow-band CCD images of the HHL 73 field were made on 2006 August 5 at the 2.6 m Nordic Optical Telescope (NOT) (ORM, La Palma, Spain) using the Service Time facility. The images were obtained with the Andalucía Faint Object Spectrograph and Camera (ALFOSC). The image scale was 0.188 arcsec pixel⁻¹. The effective imaged field was $\sim 5 \times 5$ arcmin². Images were obtained through filters of $H\alpha$ (central wavelength, $\lambda_c = 6564$ Å, bandpass $\Delta\lambda = 33$ Å, which mainly includes emission from this line, although some contamination from $[N\ II]$ emission is also present) and $[S\ II]$ ($\lambda_c = 6725$ Å, $\Delta\lambda = 60$ Å), which includes the two red $[S\ II]$ lines. The integration time was 1800 s in $H\alpha$ and 2400 s in $[S\ II]$. The seeing was 0.6–0.8 arcsec. In order to check whether there is significant continuum contribution to the HHL 73 red emission, additional exposures (600 s integration time) were acquired through a narrow-band, off-line filter, but no continuum signal around the HHL 73 location was detected. All the images were processed with the standard tasks of the IRAF¹ reduction package. Astrometric calibration of the two final images was performed. In order to register the images, we used the coordinates from the *USNO* Catalogue² of eight field stars well distributed on the observed field. The rms of the transformation was 0.12 arcsec in both coordinates.

In addition to the NOT images, we also show in Fig. 1 a CCD image of the HHL 73 field obtained on 2003 December 15 at the 2.5 m Isaac Newton Telescope (INT) through a narrow-band filter of central wavelength $\lambda_c = 6564$ Å and bandpass $\Delta\lambda = 50$ Å that also includes emission from the $[N\ II] \lambda\lambda 6548, 6583$ Å lines. The integration time was 3600 s. Astrometric calibration of this image was also performed with an accuracy of a fraction of the pixel size (0.24 arcsec rms in both coordinates). This image has a spatial resolution significantly lower than that of the NOT images since the image scale was 0.54 arcsec pixel⁻¹ and, in addition, it was obtained under worse seeing conditions (≥ 3 arcsec). However, the INT image is deeper than the NOT images and has been used in our study to look for faint emission nebulae in the field that might be related to the HHL 73 object and/or with HH 379.

2.2 Radio continuum and H_2O maser emission

We observed the 3.6 cm continuum emission towards HHL 73 with the Very Large Array of the NRAO³ in the C configuration during

¹ IRAF is distributed by the National Optical Astronomy Observatories, which are operated by the Association of Universities for Research in Astronomy, Inc., under cooperative agreement with the National Science Foundation.

² The *USNOFS* Image and Catalogue Archive is operated by the United States Naval Observatory, Flagstaff Station.

³ The National Radio Astronomy Observatory is operated by Associated Universities Inc., under cooperative agreement with the National Science Foundation.

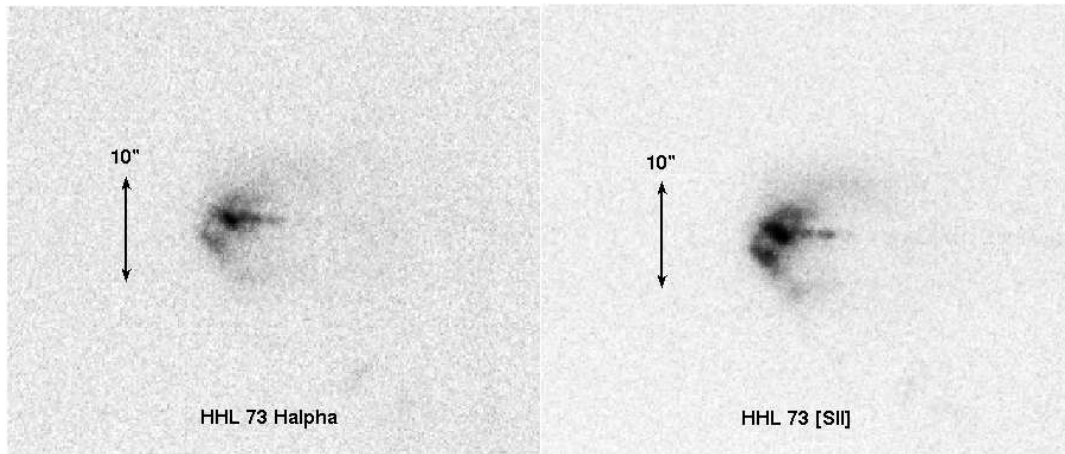


Figure 2. Close-up of the HHL 73 images obtained at the Nordic Optical Telescope (NOT, ORM) through the line filters of H α (left) and [S II] (right). In both images, the spatial structure of HHL 73 emission is resolved into two components. A microjet of ~ 4 arcsec is also visible in the two band images. The FOV of each image is $\sim 50 \times 42$ arcsec 2 . North is up and east is to the left.

1997 August 14. The phase centre was located at RA($J2000$) = $21^{\text{h}}45^{\text{m}}10^{\text{s}}.46$; Dec.($J2000$) = $+47^{\circ}33'21''.2$. The phase calibrator used was 2202+422, and the bootstrapped flux density obtained was 3.69 ± 0.07 Jy. The absolute flux density calibrator was 00137+331 (3C48), for which a flux density of 3.15 Jy was adopted. Clean maps were obtained using the task MAPPR of AIPS with the robust parameter set equal to 5, which is close to natural weighting. Since the signal-to-noise ratio of the longest baselines was low, we applied a (u, v) -taper function of 50 k λ . The resulting synthesized beam size was 4.7×4.3 arcsec 2 (P.A. = -78°), and the achieved 1σ noise level was $20 \mu\text{Jy beam}^{-1}$.

VLA archive observations of the water maser line at 22.2351 GHz ($6_{16}-5_{23}$ transition) carried out in the B configuration during 1994 July 4 were analysed. The phase centre was located at RA($J2000$) = $21^{\text{h}}45^{\text{m}}08^{\text{s}}.37$; Dec.($J2000$) = $+47^{\circ}32'49''.1$. The bootstrapped flux obtained for the phase calibrator 2202+422 was 3.08 ± 0.09 Jy, and the adopted flux density for the absolute flux calibrator (3C48) was 1.13 Jy at 1.3 cm. The observations were made using the 2IF mode, with a bandwidth of 6.30 MHz with 31 channels of 203 kHz resolution (2.66 km s^{-1} at 1.3 cm) centred at -2 km s^{-1} , plus a continuum channel that contains the central 75 percent of the bandwidth. The synthesized beam was 0.36×0.31 arcsec 2 (P.A. = -11°), and the 1σ noise level per spectral channel achieved with natural weight was 8 mJy beam^{-1} .

2.3 Integral Field Spectroscopy (IFS)

Observations of the HHL 73 object were made on 2004 November 22 with the 3.5 m telescope of the Calar Alto Observatory (CAHA). Data were acquired with the Integral Field Instrument Potsdam Multi-Aperture Spectrophotometer PMAS (Roth et al. 2005) using the PPAK configuration that has 331 science fibres, covering a hexagonal FOV of 74×65 arcsec 2 with a spatial sampling of 2.7 arcsec per fibre. In addition, PPAK comprises 36 fibres to sample the sky, located ~ 90 arcsec from the centre, packed in small bundles of six fibres each one, and distributed at the edges of the science hexagon. Fifteen calibration fibres are interpolated in between the science and sky ones in the pseudo-slit, and connected directly to the PMAS internal calibration unit (Kelz et al. 2006). The I1200 grating was used, giving an effective sampling of 0.3 \AA pix^{-1} ($\sim 15 \text{ km s}^{-1}$ for H α) and covering the wavelength range

$\sim 6500-7000 \text{ \AA}$, thus including characteristic HH emission lines in this wavelength range (H α , [N II] $\lambda\lambda 6548, 6584 \text{ \AA}$ and [S II] $\lambda\lambda 6717, 6731 \text{ \AA}$). The spectral resolution (i. e. instrumental profile) is $\sim 2 \text{ \AA FWHM}$ ($\sim 90 \text{ km s}^{-1}$) and the accuracy in the determination of the position of the line centroid is $\sim 0.2 \text{ \AA}$ ($\sim 10 \text{ km s}^{-1}$ for the strong observed emission lines). We made a single pointing of 1800-s exposure time centred on the SIMBAD position of HHL 73 (RA($J2000$) = $21^{\text{h}}45^{\text{m}}08^{\text{s}}.1$, Dec.($J2000$) = $+47^{\circ}33'6''$) covering the whole optical emission of the object (~ 30 arcsec).

Data reduction was performed using a preliminary version of the R3D software (Sánchez 2006), in combination with IRAF and the Euro3D packages (Sánchez 2004). The reduction consists of the standard steps for fibre-based integral field spectroscopy. A master bias frame was created by averaging all the bias frames observed during the night and subtracted from the science frames. The location of the spectra in the CCD was determined using a continuum-illuminated exposure taken before the science exposures. Each spectrum was extracted from the science frames by co-adding the flux within an aperture of five pixels along the cross-dispersion axis for each pixel in the dispersion axis, and stored it in a row-stacked-spectrum (RSS) file (Sánchez 2004). At the date of the observations we lacked a proper calibration unit for PPAK. Therefore, the wavelength calibration was performed iteratively. First, we illuminated the science fibres using dome *strahler* lamps with the telescope at the location of the objects. These lamps have well defined emission lines in the wavelength range considered, although the line elements and wavelength are ignored at this step. These exposures were used to correct for distortions in the wavelength solution, fixing all the spectra to a common (ignored) solution. After that, the wavelength solution was found using HgNe lamps that illuminated only the calibration fibres. Differences in the fibre-to-fibre transmission throughput were corrected by comparing the wavelength-calibrated RSS science frames with the corresponding continuum illuminated ones. The final wavelength solution was set by using the sky emission lines found in the observed wavelength range. The achieved accuracy for the wavelength calibration was better than $\sim 0.1 \text{ \AA}$ ($\sim 5 \text{ km s}^{-1}$). Observations of a standard star were used to perform a relative flux calibration. A final datacube containing the 2D spatial plus the spectral information of HHL 73 was then created from the 3D data by using Euro3D tasks to interpolate the data spatially until

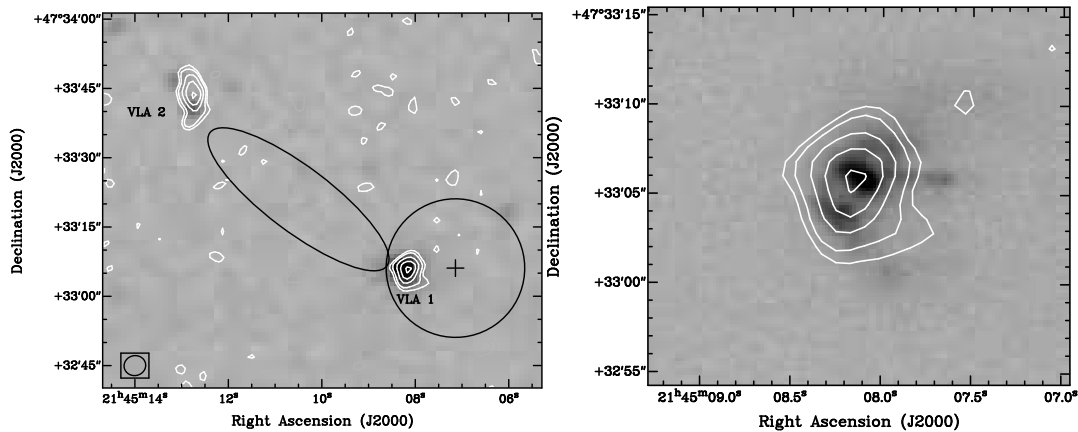


Figure 3. *Left panel:* Continuum emission at 3.6 cm (white contours) overlaid on the *K*-band 2MASS image (grey scale). The cross marks the position of the H₂O maser detected by Gyulbudaghian, Rodríguez & Mendoza-Torres (1987). The synthesized beam is shown at the bottom left corner, and the black ellipse indicates the *IRAS* error ellipse. *Right panel:* Detail of the 3.6 cm continuum emission towards HHL 73 (white contours) overlaid on the [S II] image (grey scale). In both panels, contours levels are $-5, -3, 2, 3, 5, 7,$ and 9 times the rms of the map, $20 \mu\text{Jy beam}^{-1}$.

reaching a final grid of 2.16 arcsec of spatial resolution and 0.3 Å of spectral resolution. Further manipulation of this datacube, devoted to obtaining integrated emission line maps, channel maps and position-velocity maps, were made using several common-users tasks of STARLINK, IRAF and GILDAS astronomical packages and IDA (García-Lorenzo, Acosta-Pulido & Megias-Fernández 2002), a specific suit of IDL software for analysing 3D data.

3 RESULTS

3.1 Narrow-band CCD images

Figure 1 shows the H α image of the HHL 73 field obtained at the INT. The HHL 73 object appears projected on a dark cloud near its southwestern border. The object presents in this H α image the comet-shaped morphology already found in the *DSS* plates. Because of the low effective spatial resolution of the image resulting from both the pixel scale and the seeing, we were unable to resolve any structure in the morphology of the H α emission. Neither were we able to elucidate from this image whether the emission of HHL 73 originates mainly from scattered starlight from an embedded point-source, as suggested by Devine, Reipurth & Bally (1997), or whether the emission mainly arises from gas photoionized or shock-excited by an external source. The error ellipse of *IRAS* 21432+4719 does not encompass HHL 73. From the astrometry performed on the H α image, we derived that the *IRAS* catalogue position is ~ 30 arcsec northeast of the HHL 73 H α emission peak (~ 0.13 pc for a distance of 900 pc). A 2MASS source is found very close to HHL 73 (there is an offset of ~ 1.5 arcsec between the position given for the infrared source in the 2MASS catalogue and the position of the H α emission peak of HHL 73). The nebulosities cited by Devine, Reipurth & Bally (1997) as HH 379 are also visible in our INT image close to a bright field star (see Fig. 1). However, despite a careful inspection of the HHL 73 field imaged in H α , we were unable to identify any other nebular emission suggestive of being part of a putative optical jet related to HH 379.

The narrow-band H α and [S II] images obtained at the NOT have less depth than the INT image. However the higher spatial resolution achieved in the NOT images make them suitable for resolving the structure of the HHL 73 object. Fig. 2 shows the close-up of the NOT images including the HHL 73 object in the H α (right)

and [S II] (left) bands. As can be seen from the figure, these images allow us to resolve several components in the emission of HHL 73: the comet-shaped morphology detected in the optical INT images of lower spatial resolution now appears split into two components of different surface brightness with a darker lane between them. The estimated distance between the peaks of the two HHL 73 components is ~ 2.5 arcsec (~ 0.01 pc for a distance of 900 pc). In addition, a lower brightness and more collimated emission tail, showing a couple of brightness enhancements suggestive of the “knots” of a microjet, emanates from the brighter northwestern component and extends ~ 4 arcsec towards the west at P.A. = 267° . All these HHL 73 components are found in both NOT images. However, some differences are appreciated when the emission from the two bands is compared: the northwestern component is the brighter one in both filters, H α and [S II]. The southeastern component appears dimmer, as compared with the northwestern one, in H α than in [S II]. The emission tail is brighter and has higher collimation in [S II] than in H α (as would be expected from a jet). Furthermore, while the emission peak positions of H α and [S II] are coincident in the southeastern component, the H α peak position in the northwestern component is offset by ~ 0.8 arcsec towards the southwest from the [S II] emission peak position. Thus, differences in the excitation conditions between the two HHL 73 components might be present.

Finally, note that the position angle of HH 379, as seen from HHL 73, is 262° (Davis et al. 2001, 2003), close to that of the HHL 73 microjet. Thus, although the deep INT H α image does not show any other nebulosity connecting both emissions, HH 379 could form part of the HHL 73 optical outflow, provided that the outflow direction undergoes a bending of $\sim 5^\circ$, as seen in other optical outflows propagating in an inhomogeneous medium (López et al. 1995).

3.2 Centimetre continuum and H₂O maser emission

In order to complement the CCD and IFS data of HHL 73, we analysed the data of the emission at radio wavelengths available for the HHL 73 field.

Table 1. Parameters of the continuum sources detected in the HHL 73 region.

Source	Position		Flux density ^a (mJy)	Deconv. size (arcsec)	P.A. (deg)
	$\alpha(J2000)$	$\delta(J2000)$			
VLA 1 (HHL 73)	21 ^h 45 ^m 08 ^s .15	47°33′05″.6	0.26±0.02	3.6×2.0	170
VLA 2	21 ^h 45 ^m 12 ^s .77	47°33′43″.6	0.33±0.03	7.5×0.0	9

^a Corrected for primary beam response.

3.2.1 Centimetre continuum emission

Figure 3 (left panel) shows the continuum map at 3.6 cm towards HHL 73 overlaid on the *K*-band 2MASS image. We detected two centimetre sources, VLA 1 and VLA 2, separated ~ 47 arcsec (0.2 pc in projection at the distance of the source), located near the catalogue position of *IRAS* 21432+4719. Both centimetre sources are also associated with 2MASS point sources. In Table 1 we list the positions, flux densities and deconvolved sizes of the detected sources in the HHL 73 region. In Fig. 3 (right panel) we show the 3.6 cm centimetre continuum emission arising from the HHL 73 object overlaid on the [S II] image. The peak position of the centimetre source VLA 1 is close (~ 0.7 arcsec south) to the position of the [S II] emission peak. The centimetre emission from the HHL 73 object is slightly elongated towards the secondary peak detected in the [S II]-band images to the southeast.

3.2.2 H₂O maser emission

In 1985 H₂O maser emission was detected towards HHL 73 by Gyulbudaghian, Rodríguez & Mendoza-Torres (1987) using the 37 m radio telescope of the Haystack Observatory. The H₂O maser was located 10.2 arcsec west of the HHL 73 object, with a positional uncertainty that can be estimated at ~ 15 arcsec, making it difficult to ascertain whether or not the maser is associated with HHL 73. In the archive observations analysed here we did not detect H₂O maser emission towards HHL 73 above a 6σ limit, indicating that at the epoch of observation (1994 July) the maser was out. The upper limit estimated for the peak intensity of the H₂O maser emission was 48 mJy beam⁻¹, corresponding to a main beam brightness temperature upper limit $T_{\text{MB}} = 1000$ K.

3.3 IFS: Integrated line-emission maps

3.3.1 Emission line images

We detected emission from characteristic HH lines within the observed wavelength range (H α , [N II] $\lambda\lambda$ 6548, 6584 Å and [S II] λ 6717, 6731 Å). Narrow-band images for these lines were generated from the datacube. For each position, the flux of the emission line was obtained by integrating the signal over the whole wavelength range covered by the line and subtracting a continuum obtained from the wavelengths adjacent to the emission line.

The narrow-band maps of HHL 73 obtained are shown in Fig. 4. As can be seen from the panels of the figure, the emission has a similar morphology in all the mapped lines. However it should be noted that the H α emission is slightly more extended (~ 3 arcsec) towards the south than the emission from the other lines. Furthermore, the [N II] emission appears more compact than the H α and [S II] emission. This is mostly because the [N II] emission has a lower surface brightness, and the collimated emission extending

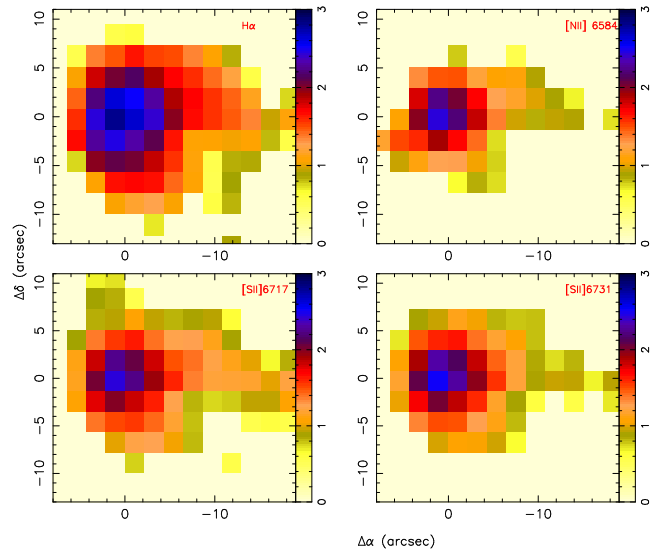


Figure 4. Integrated maps of the HHL 73 emission obtained from the datacube by integrating the signal within the wavelength range including the corresponding line labelled in each panel (H α : λ 6557.7–6569.1 Å, [N II]: λ 6579.6–6585.9 Å, [S II] λ 6716: 6712.1–6719.3 Å and [S II] λ 6731: 6728.0–6733.8 Å). Fluxes are displayed on a logarithmic scale, in units of 10^{-16} erg s⁻¹ cm⁻². The offsets of the spatial scale are relative to the position of the emission peak.

towards the west of the HHL 73 main body is hardly detected in the [N II] lines.

It should also be noted that the overall morphology derived from the H α and [S II] IFS images is in good agreement with the morphology found from the INT CCD image. In particular, the IFS images also show the low-brightness and more collimated emission feature originating west of the HHL 73 main body. However, the lower spatial resolution of the IFS images did not allow us to resolve the two components of the HHL 73 main body discovered from the H α and [S II] NOT images.

3.3.2 Kinematics

In addition to the integrated flux, we derived for each position the flux-weighted mean radial velocity⁴ $\langle V \rangle$, and the flux-weighted rms width of the line $(\Delta V^2)^{1/2}$, proportional to the FWHM, which are given by

⁴ All the velocities in the paper are referred to the local standard of rest (LSR) frame. A $V_{\text{LSR}} = +3.6$ km s⁻¹ for the parent cloud has been taken from Dobashi et al. (1993).

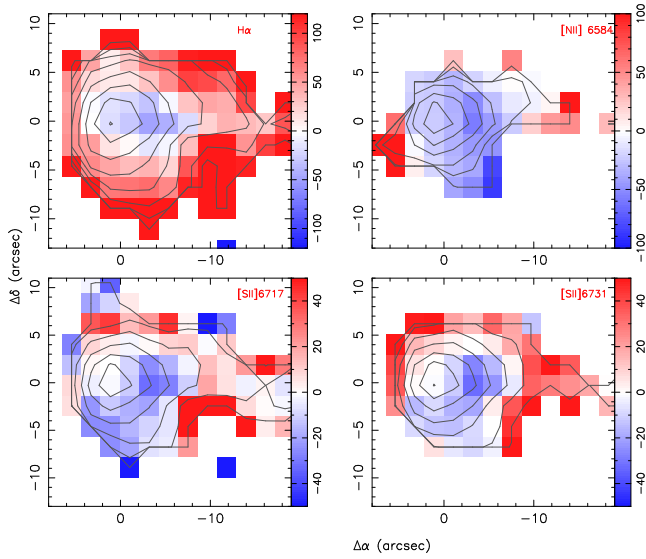


Figure 5. Flux-weighted mean velocity maps. Velocities (km s^{-1}) are referred to the V_{LSR} of the parent cloud. The offsets of the spatial scale are relative to the position of the emission peak. Contours of the integrated flux of the corresponding line have been overlaid. The lowest contour level is $7 \times 10^{-17} \text{ erg s}^{-1} \text{ cm}^{-2}$ and the contour spacing is $3 \times 10^{-17} \text{ erg s}^{-1} \text{ cm}^{-2}$.

$$\langle V \rangle = \frac{1}{I} \int_{\text{line}} I_V V dV \quad (1)$$

and

$$\Delta V^2 = \frac{1}{I} \int_{\text{line}} I_V (V - \langle V \rangle)^2 dV, \quad (2)$$

where

$$I = \int_{\text{line}} I_V dV \quad (3)$$

In spite of the spatial extension of the emission being quite compact, the velocity field derived for $\langle V \rangle$ appears rather complex for all the lines and shows appreciable changes through HHL 73, as can be seen from Figure 5.

For all the mapped lines, the gas appears blueshifted around the emission peak, with $\langle V \rangle$ values of -20 km s^{-1} for $\text{H}\alpha$ and $[\text{N II}]$, and -2.0 km s^{-1} for the $[\text{S II}]$ lines. However, the highest blueshifted velocities are found $\sim 5 \text{ arcsec}$ west of the emission peak position, where values of -50 km s^{-1} for $\text{H}\alpha$ and $[\text{N II}]$, and -32.0 km s^{-1} for the $[\text{S II}]$ lines have been derived.

The FWHM values obtained from the $(\Delta V^2)^{1/2}$, corrected from the instrumental profile, are high for all the mapped lines. Around the emission peak position, FWHMs are $\sim 190 \text{ km s}^{-1}$ for the $\text{H}\alpha$ line and $\sim 100 \text{ km s}^{-1}$ for the $[\text{N II}]$ and $[\text{S II}]$ lines. These values are representative of the FWHMs found in the whole emitting region, although the FWHMs slightly increase towards the southeast and decrease towards the west from the emission peak position. Such large line widths might be indicating turbulent gas motions, which are more important close to the position proposed by Davis et al. (2001, 2003) for an unseen embedded exciting source. Another possibility is that the high FWHM values derived were due to the contribution of several kinematic components of the line profiles. We shall analyse this possibility later by using a multicomponent line profile model to fit the $[\text{S II}]$ profiles.

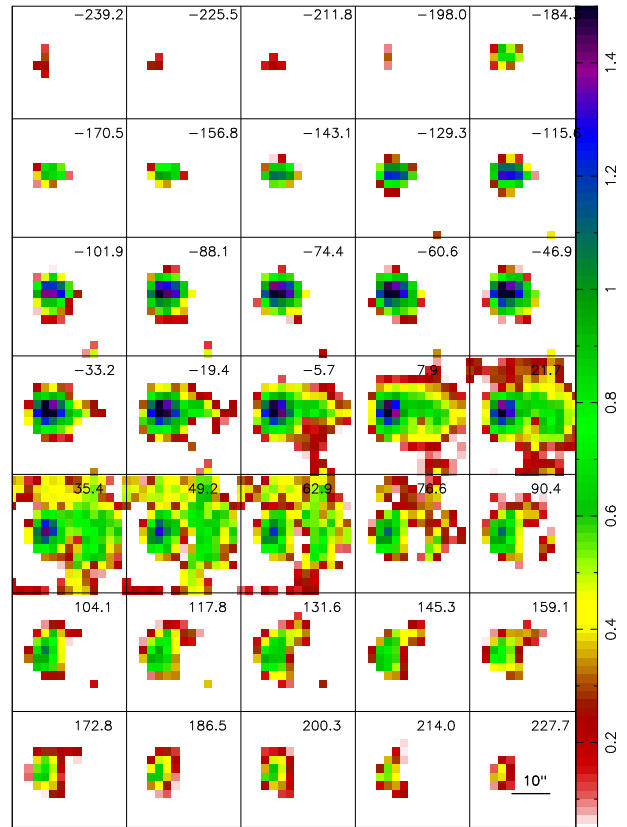


Figure 6. $\text{H}\alpha$ channel maps centred on the V_{LSR} radial velocities (km s^{-1}) labelled in each panel. The spatial scale is given in one of the panels. Fluxes have been displayed on a logarithmic scale, in units of $10^{-16} \text{ erg s}^{-1} \text{ cm}^{-2}$. (Channels corresponding to $+21.7 \leq V_{\text{LSR}} \leq +62.9$ are affected by residuals of an inaccurate subtraction of the sky background at the north of the emission).

3.3.3 Physical conditions

Line-ratio maps of the integrated line fluxes are suitable for getting spatial information about excitation conditions (from $[\text{S II}]/\text{H}\alpha$, $[\text{N II}]/\text{H}\alpha$) and electron density (from $[\text{S II}] 6717/6731$) of the emitting gas. For the entire region covered by the compact bright HHL 73 emission, the derived $[\text{S II}] 6717/6731$ line ratios go from ~ 0.6 to ~ 0.9 , indicating a range of electron densities $n_e = 900\text{--}4000 \text{ cm}^{-3}$, the highest values being reached around the emission peak position. Electron density lowers towards the west in the low-brightness collimated emission tail (e. g. $[\text{S II}] 6717/6731$ line ratio ~ 1 , corresponding to $n_e \simeq 600 \text{ cm}^{-3}$, is derived at a position $\sim 5 \text{ arcsec}$ west of the peak position). These values were derived for $T_e = 10^4 \text{ K}$.

The derived $[\text{S II}]/\text{H}\alpha$, $[\text{N II}]/\text{H}\alpha$ line ratio distributions show a similar pattern. Both line ratios peak around the emission peak position, with $[\text{S II}]/\text{H}\alpha \simeq 0.9$ and $[\text{N II}]/\text{H}\alpha \simeq 0.4$. Line ratios decrease steeply (excitation increases) southeast of the peak, while the decrease is slower to the west along the low-brightness emission tail.

3.4 IFS: Channel maps

An inspection of the HHL 73 spectra at different positions revealed that the line profiles, being broad and asymmetric, display a variety of features suggesting complex gas kinematics.

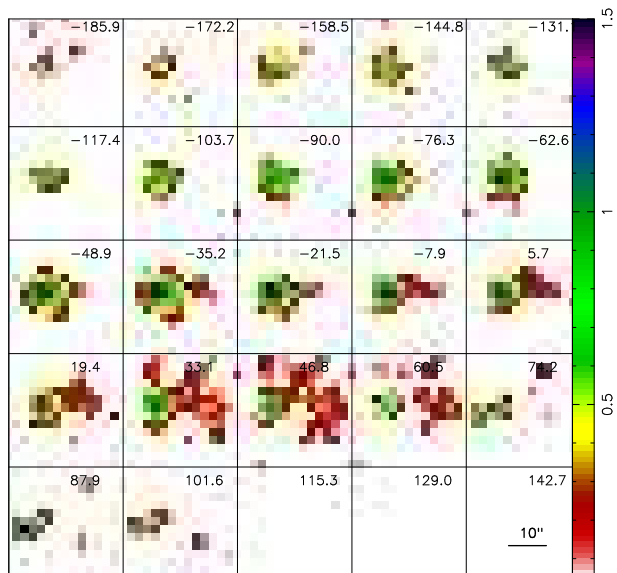


Figure 7. Same as Fig. 6, but for [N II] $\lambda 6584$ Å.

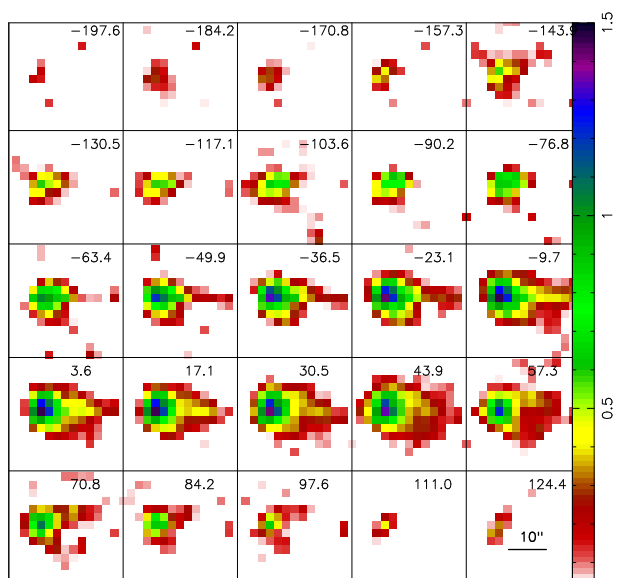


Figure 8. Same as Fig. 6, but for the [S II] 6717 Å emission line.

We will now analyse the behaviour of the emission as a function of velocity. First, we obtained the $H\alpha$, [N II] and [S II] channel maps to explore the 3D structure of the physical conditions as a function of the radial velocity. Furthermore, to analyse the complex line profiles found along the HHL 73 emission, we extracted spectra for each spaxel within the area covered by the emission and we fitted the line profiles through a multicomponent line profile model.

3.4.1 Spatial distribution of the emission

A more detailed sampling of the gas kinematics was obtained by slicing the datacube into a set of velocity channels along each emission line profile, thus providing a “tomograph” of the emission line, not restricted to the centroid of the line, but including also the wings. Each slice was made for a constant wavelength bin of 0.3 Å,

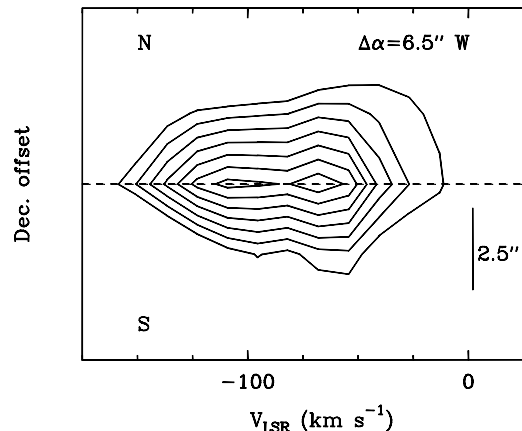


Figure 9. Position–Velocity diagram of the $H\alpha$ emission for a cut along the Dec. axis at $RA \simeq 6.5$ arcsec west of the position of the intensity peak. The $\Delta\delta = 0$ position is marked by the dashed line. The contour spacing is 10 per cent of the peak intensity.

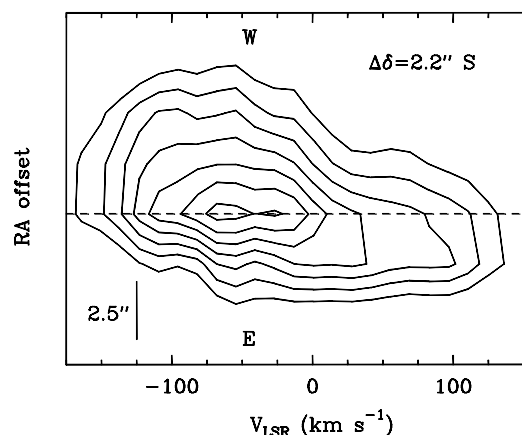


Figure 10. Position–Velocity diagram of the $H\alpha$ emission for a cut along the RA axis at Dec. $\simeq 2.2$ arcsec south of the position of the intensity peak. The $\Delta\alpha = 0$ position is marked by the dashed line. The contour spacing is 10 per cent of the peak intensity.

corresponding to a velocity bin of ~ 14 km s^{-1} . The channel maps obtained for $H\alpha$, [N II] $\lambda 6584$ Å and [S II] $\lambda 6717$ Å are shown in Figs 6, 7 and 8 respectively. As we used the same wavelength bin for all the lines, the central velocity of a given channel map differs slightly from a line to another.

As can be seen from Figs 6 and 8, the spatial distribution of the $H\alpha$ and [S II] emission found from the line-integrated IFS maps (i. e. the compact, bright region that extends towards the west in a low-brightness and collimated tail) is also found in all the velocity channel maps ranging from blueshifted V_{LSR} velocities of -30 km s^{-1} up to redshifted velocities of $+20$ km s^{-1} in both emission lines.

The emission spreads over a wide velocity range for all the mapped lines, the span of the velocity range being slightly different for each line. The $H\alpha$ emission extends over the widest range as compared with the other lines, covering a range ~ 400 km s^{-1} wide, from -185 to $+200$ km s^{-1} . The strongest and more extended $H\alpha$ emission is found for the velocity channels ranging from -50 to $+20$ km s^{-1} . The [S II] emission is detected within a velocity range ~ 250 km s^{-1} wide, from -145 to $+100$ km s^{-1} . The strongest and more extended [S II] emission is found for the veloc-

ity channels ranging from -50 to $+45$ km s^{-1} . The [N II] emission is detected within a velocity range ~ 300 km s^{-1} wide, from -170 to $+105$ km s^{-1} . The [N II] emission presents a similar spatial extension in most of the velocity channels since the low-brightness emission tail is hardly detected in the [N II] line.

Furthermore, we performed position–velocity (*PV*) diagrams at different right ascension and declination positions, both in the $\text{H}\alpha$ and [S II] lines. Two of these $\text{H}\alpha$ cuts at selected positions are shown in order to illustrate more clearly a trend found in the velocity distribution of the emission.

Figure 9 shows the *PV* diagram obtained for a cut at RA $\simeq 6.5$ arcsec west of the position of the emission peak (marked in the figure by a dashed line). This cut along the declination axis has been done at an RA position that intersects the beginning of the collimated emission tail. The figure clearly shows that the overall emission appears blueshifted north and south of the emission peak, at $V_{\text{LSR}} \simeq -110$ km s^{-1} . Another velocity component is also found peaking at ~ -70 km s^{-1} . Furthermore, note that the spatial distribution of the velocities is slightly asymmetric, with the range of velocities increasing from north to south: e. g. the velocities range from -130 to -15 km s^{-1} at ~ 2 arcsec north of the emission peak, while the velocities range from -110 to -45 km s^{-1} at ~ 2 arcsec south of the emission peak.

Figure 10 shows the *PV* diagram obtained for a cut at Dec. $\simeq 2.2$ arcsec south of the position of the emission peak. For this cut along the RA axis, the figure shows that there is also a clear asymmetry in the spatial distribution of velocities: the emission at blueshifted velocities is spatially more extended towards the west, while at redshifted velocities it is more extended towards the east of the peak emission position. Two blueshifted velocity components, peaking at ~ -70 and ~ -25 km s^{-1} , are also detected for this cut.

The inspection of different *PV* diagrams obtained at several positions up to ≤ 10 arcsec around the emission peak revealed a general trend, both in the $\text{H}\alpha$ and [S II] lines, in the highest blueshifted velocities appearing towards the west of the emission peak position, with the velocity values increasing from west to east along HHL 73. This signature of a two-velocity distribution in the emission can be hardly appreciated in the channel maps.

3.4.2 Density and excitation conditions

We also explored the behaviour of the density and excitation as a function of the velocity by generating the line ratio channel maps for a velocity range from -135 to $+110$ km s^{-1} .

Regarding the kinematics of the emission, the [S II] 6717/6731 line-ratio channel maps indicate that n_e decreases with increasing velocities: the blueshifted gas has higher n_e than the redshifted gas. This trend is found at different position along the HHL 73 emission. Around the position of the emission peak, we derived $n_e \simeq 2200$ cm^{-3} for the -80 km s^{-1} velocity channel, while $n_e \simeq 740$ cm^{-3} is derived for the -55 km s^{-1} velocity channel.

Regarding the spatial distribution of the emission, the [S II] 6717/6731 line ratio channel maps indicate that n_e decreases from east to west for all the velocity channels, the n_e variations being different depending on the velocity. In fact, the variations found for n_e along the east–west axis seem to decrease with increasing velocity: e. g. in the -80 km s^{-1} channel, n_e changes from ~ 4200 to ~ 740 cm^{-3} (i. e. a factor of ~ 5) as we move ~ 10 arcsec from east to west; in contrast, n_e only changes from ~ 1400 to ~ 490 cm^{-3} for the same spatial displacement in the $+82$ km s^{-1} channel.

The [S II]/ $\text{H}\alpha$ line-ratio channel maps show an increasing

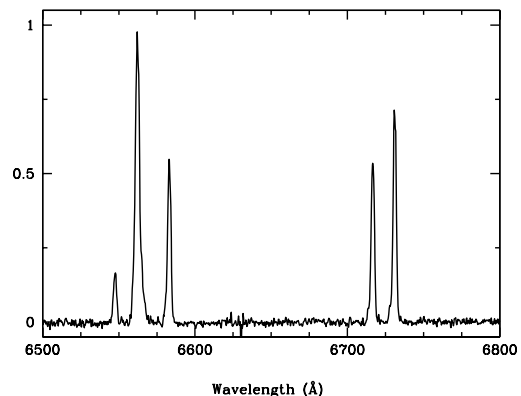


Figure 11. Spectrum extracted at the emission peak position. Flux has been normalized to the flux of the $\text{H}\alpha$ peak. The characteristic HH emission lines ($\text{H}\alpha$, [N II] $\lambda 6548$, 6583 Å and [S II] $\lambda 6717$, 6731 Å) are clearly seen.

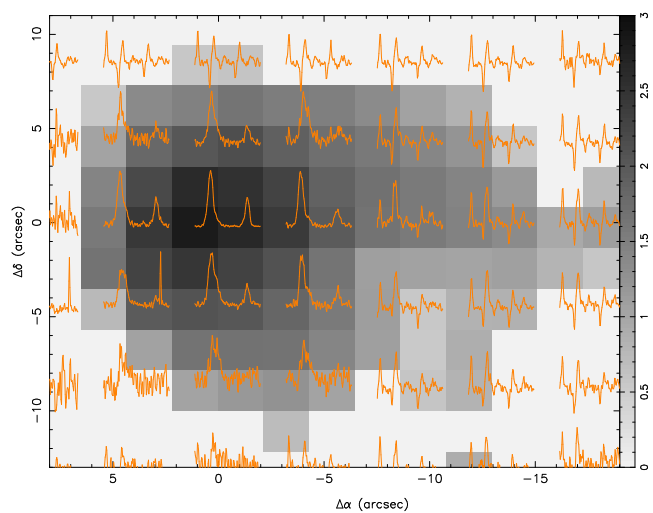


Figure 12. Two-dimensional distribution diagram of the observed spectra in the spectral window 6553.1 – 6590.7 Å, including the $\text{H}\alpha$ and [N II] $\lambda 6584$ Å lines. Each spectrum has been obtained by averaging the spectra within an aperture of 2×2 spaxels ($\sim 4 \times 4$ arcsec 2) and its intensity has been normalized to the $\text{H}\alpha$ peak. Spectra are overlaid on the $\text{H}\alpha$ integrated map obtained as in Fig. 4.

trend (i. e. decreasing excitation) with increasing velocity, from blueshifted velocities up to a velocity of $\sim +40$ km s^{-1} . For higher redshifted velocities, line-ratio values decrease (i. e. excitation increases). Thus the behaviour derived from the line ratios is that the excitation is higher at high absolute velocity values (both blueshifted and redshifted) than at low (absolute) velocity values.

Regarding the spatial distribution, the general trend found for each velocity channel is a decrease in the line ratios (i. e. an increase of excitation) from east to west.

3.5 IFS: Line-profile multicomponent analysis

Figure 11 shows the spectrum extracted at the $\text{H}\alpha$ emission peak position. As can be seen in the figure, the spectrum is closely reminiscent of the characteristic shock-excited HH spectra. Note in addition that the line profiles are broad and asymmetric, suggesting that multiple kinematic components are contributing to the line profile. Furthermore, the inspection of the spectra extracted at different positions over HHL 73 reveals that the line profiles display a variety

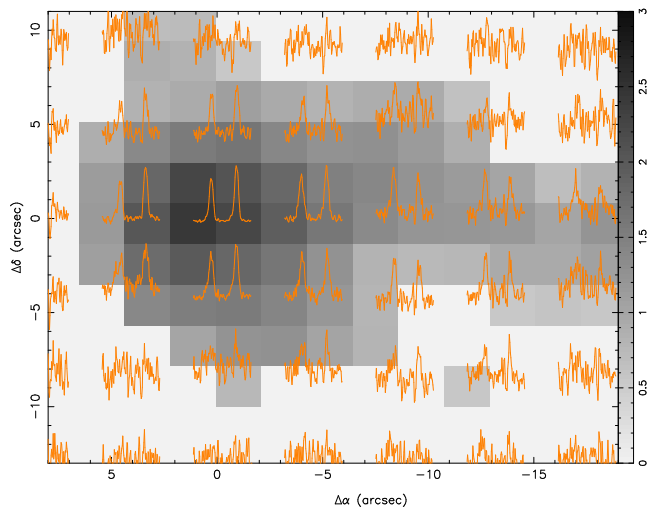


Figure 13. Same as Fig. 13, but for the [S II] emission. The spectral window selected for this plot is 6706.4–6739.5 Å.

of features. Around the emission peak, line profiles are asymmetric and broad, with a faint blue double peak suggesting the presence of several gaseous systems. To the north and south of the emission peak, the profiles clearly have contributions from at least two components, showing double peaks and/or broad wings. Towards the west of the emission peak, in the low-brightness collimated emission tail, the line profiles are more complex, showing blue and red shoulders as well as broad wings. All the emission lines in the observed spectral range show similar features to those described here, as can be seen in Figs 12 and 13, where the spectra for the spectral ranges which include the H α and [N II] λ 6584 Å (Fig. 12) and the [S II] λ 6717, 6731 Å emission lines (Fig. 13) have been overlaid on the flux maps obtained by integrating the signal within the same spectral range.

The complex line-profile pattern appears in both the H α and in the [S II] lines. We used the [S II] lines to perform a line-profile decomposition to reproduce the profiles of the HHL 73 spectra, since the [S II] emission should be less contaminated from the emission of a putative, undetected source and thus, should better trace the kinematics of the shock-excited outflow gas. The [S II] line profiles were well reproduced by assuming the contribution from three kinematic components. The line-profile decomposition was obtained from a model including three Gaussian components. The Gaussian fitting was performed using the DIPSO package of the STARLINK astronomical software. The wavelength difference between the two [S II] lines was fixed according to their corresponding atomic parameters. Furthermore, the same FWHM of the Gaussian in each of the two [S II] lines was assumed for each component of the profile.

According to the fit parameters, we identified three Gaussians with three different kinematic components well-separated in velocity (wavelength), as shown in Fig. 14: two of the velocity components are blueshifted and the third is redshifted. In the following, we refer to the blueshifted high-velocity component as BHVC (filled triangles in the figure), to the blueshifted low-velocity component as BLVC (open dots) and to the redshifted velocity component as RVC (filled dots). Reasonably good results were obtained from this three-Gaussian components model along the whole HHL 73 emission (see Fig. 15 for some examples, where the fits obtained at selected positions and their residual are plotted). The V_{LSR} velocities of the BHVC range from -140 to -90 km s $^{-1}$,

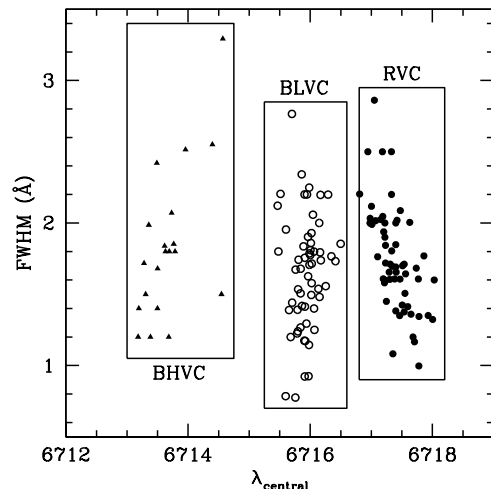


Figure 14. Central wavelength vs. FWHM for all the lines obtained by fitting the HHL 73 spectra to a three Gaussian model. Symbols denote the so-called BLVC (open dots), RVC (filled dots) and BHVC (filled triangles) velocity components (see text).

with values increasing towards the south. At the peak of the emission, the BHVC reaches a value of -100 km s $^{-1}$. The velocities of the BLVC range from -50 to -2 km s $^{-1}$, with -20 km s $^{-1}$ at the peak of the emission, with values increasing towards the east. Finally, the velocities of the RVC range from $+20$ to $+40$ km s $^{-1}$, with $+35$ km s $^{-1}$ at the peak of the emission. The highest values of the RVC are found around the emission peak, and the velocity decreases towards the edges of HHL 73.

The line-profile decomposition also shows significant differences, both in the spatial distribution and in the relative strength of the emission associated with each of the three velocity components (see Fig. 16, where the flux contours of each kinematic component are overlaid on the [S II]-band NOT image). Regarding the spatial distribution, the BLVC and RVC components are present in almost all the spectra, while the BHVC component is concentrated in a smaller region, west of the emission peak. Regarding the relative strength of the components, the emission from the BHVC is the weakest (with flux values roughly one third of those found in the other components). The strongest emission comes from the BLVC component. Finally, the emission with the widest spatial distribution comes from the RVC, the strength of its emission being slightly weaker than that of the BLVC.

Interestingly, we found a significant spatial displacement among the positions of the emission peaks of the three velocity components (see also Figure 16). The emission peaks of the BLVC and RVC components are closely coincident (the estimated offset between the peaks of both components is ~ 1.3 arcsec; note that the IFS pixel size is 2.16 arcsec). In contrast, the BHVC peaks ~ 3.7 arcsec northwest of them. As can be seen in Fig. 16, the emission from the redshifted component closely reproduces the spatial distribution of the bright bow-shaped HHL 73 emission, while its contribution to the collimated, low-brightness emission tail is lower than those from the blueshifted components. The two blueshifted components appear mainly associated with the northwestern component of the bright bow-shaped HHL 73 emission and with the HHL 73 collimated emission tail. The shape of the the BLVC emission appears elongated in the east–west direction, extending towards the west, and its emission peak closely coincides with the peak of the

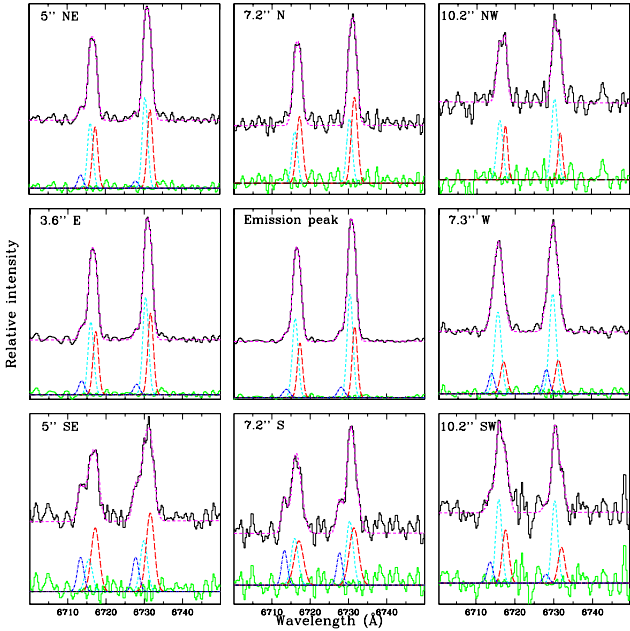


Figure 15. Observed spectra (black histograms) and fits (dashed magenta lines) obtained from the model of three Gaussian components applied to the [S II] $\lambda\lambda 6717, 6731 \text{ \AA}$ emission lines. The individual components are shown at the bottom of each panel. The same colour indicates the same component in each line. Residuals obtained subtracting the fit from the observed spectra are plotted in green. Labels in the left corner of each plot indicate the offset of each observed spectrum from the [S II] emission peak.

[S II] emission found in the narrow-band NOT images. Finally, the emission from the BHVC, located in a smaller area, also appears slightly elongated in the east–west direction, peaking ~ 4 arcsec west of the [S II] emission peak. Note however that a clear association of each kinematic component with a given morphological component of the HHL 73 [S II] emission cannot be easily derived only by looking to the [S II] channel maps, since the emission from the wings of the stronger BLVC and RVC emissions give an appreciable contribution to the emission at positions where the BHVC (the kinematics component with the weakest emission) is located (e. g. west of the peak of the emission), thus contaminating the global emission at these positions. Finally, it should be pointed out that similar kinematic structures consisting of two blueshifted (low and high) velocity components have already been detected in Class I YSO (Takami et al. 2006) and in microjets from T Tauri stars (Bacciotti et al. 2000; Lavalley-Fouquet, Cabrit & Dougados 2002).

4 DISCUSSION

4.1 The origin of the HHL 73 optical emission

In all the positions covered by the HHL 73 emission, the spectra extracted from the IFS datacube appear as low-ionization, line-emission spectra with no appreciable continuum emission, (see Figs 12 and 13). In particular, the spectrum shown in Fig. 11, corresponding to the emission of the ~ 2 arcsec region around the peak position, shows no significant continuum emission superposed on the observed lines.

We compared the [N II]/[S II] and [N II]/H α line ratio values

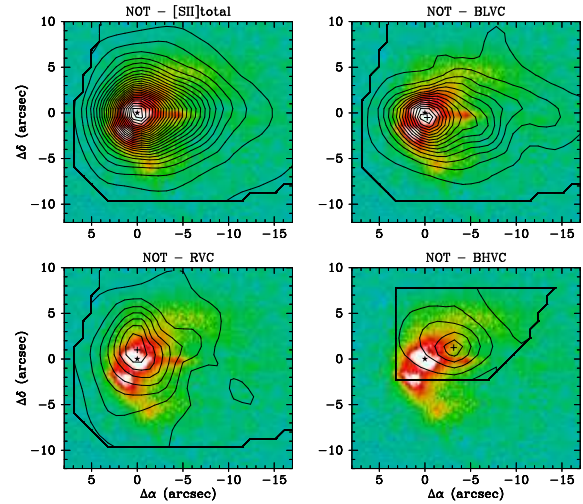


Figure 16. *Top-left:* [S II] intensity maps obtained from the fit of the three-Gaussian model to the emission line profiles and adding the individual fluxes obtained for each velocity component. *Top-right:* [S II] intensity map for the BLVC. *Bottom-left:* [S II] intensity map for the RVC. *Bottom-right:* [S II] intensity map for the BHVC. The intensity of each velocity component is overlaid on the narrow-band [S II] NOT image.

measured at several positions around the peak emission (where the signal-to-noise ratio is high enough to do the diagnostic with confidence) with those obtained from the diagnostic diagrams derived from the models of Kewley & Dopita (2002). These models give the *ionization parameter* (i. e. ionizing photon flux through an unit area) of the photoionized gas found in H II and star-forming regions as a function of the line-flux ratios for a set of metallicities. The values found for the HHL 73 [N II]/[S II] and [N II]/H α line ratios cannot be simultaneously fitted by the photoionization models: the [N II]/H α ratios are compatible with a low *ionization parameter* for metallicities $z \geq 0.5 z_{\odot}$; in contrast, for a wide range of *ionization parameters*, the [N II]/[S II] ratios are only compatible with metallicity ranges significantly lower ($0.2 \leq z \leq 0.5 z_{\odot}$). Thus, it does not seem plausible to interpret the HHL 73 optical emission as mainly originating from photoionization from a stellar source.

In contrast, the [N II]/H α and [S II]/H α line ratio values derived in HHL 73 are fully compatible with those found for HH objects (i. e. from shock-excited emission) in the current diagnostic diagrams such as those of Cantó (1981). Both HHL 73 line ratio values correspond to diagram regions where the HH objects are placed, being thus outside the regions where the spectra from photoionized nebula, such as the planetary nebula and the H II regions, are located. It should be noted that the values measured for these two line ratios (0.4–0.6 for [N II]/H α and 0.9–1 for [S II]/H α) are more compatible with the values found in HHs of high/intermediate excitation spectra than with the values found in HHs of low-excitation spectra. The degree of excitation of the HHL 73 spectra cannot be properly settled without data from the emission in a bluer wavelength range including high excitation emission lines (e. g. [O III]). Note, however, that the HH objects in which centimetre continuum emission was reported currently show a high-excitation spectrum.

Thus, the HHL 73 IFS data suggest that the emission arises mainly from shock-excited gas, characteristic of an HH object.

The contribution from continuum emission, if any, should be very weak, as derived from our optical data. We generated contin-

uum images from the IFS datacube by integrating, at each position, the signal over the wavelength range free of lines emission. In these images, we have only been able to find hints of an emission enhancement relative to the neighbouring image background around the HHL 73 position, but a at very low-level ($< 3\sigma$). In addition, the narrow-band, off-line filter NOT image fail to detect continuum emission, although it has less depth than the IFS data. This putative continuum contribution could arise from light scattered by dust better than from a point-like stellar source, as it extends over several pixels.

4.2 The origin of the near-*IR* emission associated with HHL 73

Let us discuss the nature of the *2MASS* source found near the peak position of HHL 73.

Regarding its size, the *2MASS* *J*-, *H*- and *K*-band images show that the *2MASS* source appears slightly extended when compared with other sources in the fields. Typical FWHM of the field point sources are 3.3 ± 0.2 arcsec, while the FWHMs of the *2MASS* source are 5.7, 5.3 and 4.8 arcsec in the *J*-, *H*- and *K*-bands respectively, corresponding to a deconvolved size of ~ 4 arcsec (~ 3500 AU for a distance of 900 pc).

Regarding the near-*IR* colour, the (*J* – *H*, *H* – *K*) colour-colour diagrams are commonly used to discriminate between pre-main sequence objects and field (main sequence and giant) stars (see e.g. Ojha et al. 2004). The near-*IR* colour indices of the *2MASS* source derived from the *2MASS* photometry, (*H* – *K*) = 1.26 ± 0.09 , (*J* – *H*) = 1.47 ± 0.11 , place the source inside the area corresponding to YSOs of Class II, whose near-*IR* emission originates both from a photosphere and a circumstellar disc, but its colours are also compatible, within the photometric uncertainties, with being a Class I source, having thermal emission from a circumstellar envelope. Thus, from the near-*IR* colours, it seems plausible to infer that the *2MASS* source corresponds to a very red, embedded Class II or a Class I source (i.e. a typical outflow-driving source). According to current evolutionary models of PMS stars (e.g. Palla & Stahler 1993; Siess, Dufour & Forestini 2000), the *2MASS* source lies in the region of the (*J*, *J* – *H*) colour-magnitude diagram that corresponds to low-mass YSOs with masses $\leq 1M_{\odot}$. The size derived for the *2MASS* source is compatible with that expected for an evacuated cavity around a YSO. However, in this scenario the bulk of the near-*IR* emission should mainly arise from continuum scattered starlight, and this does not seem to be the case. Davis et al. (2001, 2003) obtained high-resolution long-slit spectra at the HHL 73 position and were unable to detect continuum emission in the *H* and *K* bands including [Fe II] (at $1.64 \mu\text{m}$) and H_2 (at $2.12 \mu\text{m}$) emissions. Thus, the continuum near-*IR* emission in HHL 73, if present, is weak.

An alternative origin for the bulk of the near-*IR* emission is shock emission instead of scattered starlight. In this case, the *2MASS* *K*-band luminosity would mainly arise from the H_2 $2.12 \mu\text{m}$ line, the *H*-band luminosity from the [Fe II] $1.64 \mu\text{m}$ line, and the *J*-band luminosity from other lines, like the [Fe II] $1.25 \mu\text{m}$ line. However, this is hard to confirm, since no spectrum covering the *J*-band range is available, and the *2MASS* *K* and *H* magnitudes cannot be compared reliably with the magnitudes derived from the line fluxes given by Davis et al. (2001, 2003) – the line fluxes correspond to the integrated emission within a 0.8×2.7 arcsec, i.e. only a small fraction of the source size. In addition, the colour indices derived for the *2MASS* source are also compatible with those expected for reddened molecular shocks, as was modelled by Smith

(1995) for a wide range of shock parameters of molecular C- and J-shocks, who found that embedded shocks could mimic the near-*IR* colours derived for Class 0 sources, both sharing the same area of the near-*IR* colour diagrams. Furthermore, Davis et al. (2001, 2003), from the analysis of the kinematics derived from the near-*IR* spectra, suggest that the [Fe II] and H_2 emissions are tracing an outflow lying close to the plane of the sky, with a blueshifted component towards the west and a redshifted component towards the east.

Thus, we found no conclusive evidence for the bulk of the near-*IR* emission of the *2MASS* source close to the HHL 73 peak to be mainly tracing the scattered light from the YSO driving the outflow. Alternatively, a shock origin for the bulk of the near-*IR* emission seems to be compatible with the observations.

4.3 The origin of the centimetre emission associated with HHL 73

Centimetre continuum emission arising from HH objects has been detected in both high-mass (e.g. HH 80-81: Rodríguez & Reipurth 1989; Martí, Rodríguez & Reipurth 1993, and IRAS 16547–4247: Garay et al. 2003; Rodríguez et al. 2005) and low-mass star-forming regions (e.g. HH 1 and HH 2: Pravdo et al. 1985; Rodríguez et al. 1990, and HH 32A: Anglada et al. 1992). In high-mass star-forming regions, the centimetre emission has a negative spectral index, which is consistent with non-thermal synchrotron emission arising from shocks resulting from the interaction of a collimated stellar wind with the surrounding medium, while in low-mass star-forming regions the centimetre emission shows a flat spectrum, which is consistent with optically thin free-free thermal emission from ionized gas.

The spectral index of the centimetre HHL 73 emission cannot be derived from the present single-frequency observations. Further observations at another frequency are needed to estimate the spectral index in order to discriminate between a thermal and non-thermal origin for the centimetre emission of HHL 73. However, the exciting source of HHL 73 should be a low-/intermediate-mass YSO, since its bolometric luminosity is low (see next section). Thus, the centimetre emission detected in HHL 73 is most probably free-free thermal emission from ionized gas.

Two mechanisms could ionize the gas: photoionization or shocks. The observed flux density (Table 1), at the distance of HHL 73, corresponds to a centimetre continuum luminosity of 0.21 mJy kpc^2 . As discussed by Anglada (1995), the bolometric luminosity required to produce such a centimetre continuum luminosity by photoionization is $\sim 10^3 L_{\odot}$, more than an order of magnitude higher than the upper limit derived for the HHL 73 exciting source. In contrast, the HHL 73 centimetre continuum luminosity is typical of thermal radio-jets tracing molecular-outflow exciting sources, whose radio-continuum emission is produced by shock ionization. In addition, the momentum rate of the HHL 73 molecular outflow, derived from the CO data of Dobashi et al. (1993), fits the momentum rate vs. centimetre continuum luminosity relationship expected for shock-ionization induced emission in molecular-outflow sources of low bolometric luminosity (Anglada 1995).

In conclusion, the centimetre continuum emission of HHL 73 most probably arises from shock-ionized gas.

4.4 Is *IRAS* 21432+4719 tracing the exciting source of HHL 73?

IRAS sources in star-forming regions are frequently found tracing the driving source of molecular and atomic outflows. The *IRAS* source closest to HHL 73 is 21432+4719, whose position from the *IRAS* Point Source Catalogue is ~ 30 arcsec northeast of the HHL 73 peak position (~ 0.13 pc for a distance of 900 pc), with a large uncertainty, so that HHL 73 lies outside the *IRAS* error ellipse, near its southwestern border (see Fig. 1).

IRAS 21432+4719 is well detected in three *IRAS* bands, having a rising far-*IR* spectral energy distribution, with flux densities of 1.42, 12.19 and 23.45 Jy at 25, 60 and 100 μm respectively, and an upper limit of 0.25 Jy at 12 μm . The bolometric luminosity derived from the *IRAS* flux densities, following the recipe of Connelley et al. (2007), is $27 L_{\odot}$. This luminosity corresponds to a ZAMS star of $2.6 M_{\odot}$. The *IRAS* colours derived from the fluxes are typical of embedded protostellar sources (Beichman et al. 1986; Dobashi et al. 1992), being redder than those found for T Tau-like sources (Harris, Clegg & Hughes 1988).

Let us discuss whether *IRAS* 21432+4719 is tracing the embedded exciting source of HHL 73.

As can be seen in Fig. 1, HHL 73 lies close to the border of a region of high visual extinction. A detailed study of the brightness distribution of the optical and near-*IR* emission of HHL 73 shows that there is a shift towards the northeast of the emission centroid position with increasing wavelength. The shift between the $H\alpha$ and K -band emission centroids is ~ 1.5 arcsec, while between the J - and H -, and between the H - and K -band emission centroids it is ≤ 1 arcsec. These shifts are indicative of a large gradient of extinction, with extinction increasing towards the northeast. Thus, if there is far-*IR* emission associated with HHL 73, we expect to find it offset to the northeast of the optical and near-*IR* emissions.

As already mentioned, the catalogue position of *IRAS* 21432+4719 is offset from HHL 73 in the expected direction, although somewhat displaced from the HHL 73 position. Nonetheless, the region encompassed by the *IRAS* error ellipse, i. e. the region with the highest probability of finding the *IRAS* source, almost reaches the HHL 73 location. Thus, the far-*IR* emission could be located nearer to the optical and near-*IR* emission than the *IRAS* catalogue position.

No source is detected in the area encompassed by the *IRAS* error ellipse in the four bands of the *Midcourse Space Experiment* (*MSX*), at wavelengths from 8 to 22 μm . However, it should be noted that at 8.28 μm , in the highest-sensitivity *MSX* band, there are hints of an enhancement in emission over the local background in a few pixels covering the position of the *2MASS* source, but at a level below 3 times the image rms.

In conclusion, in spite of the angular separation between the *IRAS* source and the optical and near-*IR* emission of HHL 73, *IRAS* 21432+4719 is the most plausible candidate to be driving HHL 73, although the evidence is inconclusive and new observations in the millimetre wavelength range are needed to confirm this issue.

4.5 A speculative scenario for HHL 73

The HHL 73 morphology is reminiscent of the HH 83 system (e. g. Reipurth 1989). *IRAS* 05311–0631, the proposed exciting source of HH 83, is found located within a region with high visual extinction, close to the apex of the optical emission. The HH 83 system is interpreted as an optical jet emerging from a conical cavity

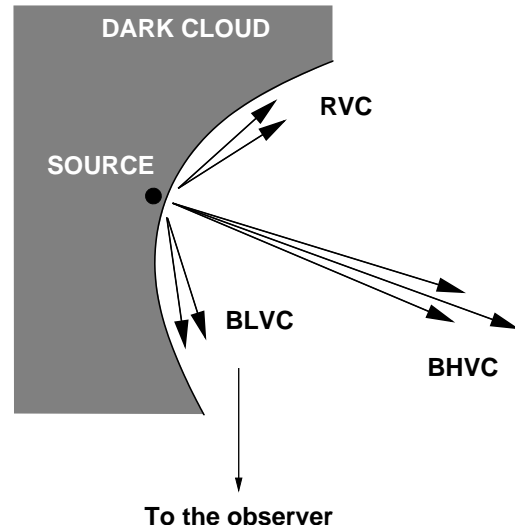


Figure 17. Sketch of the scenario proposed for HHL 73.

ity evacuated by the outflow. The counterjet is not visible since it flows inside the high-extinction region. The bulk of the bow-shaped emission at the base of the HH 83 jet arises from reflected light of the driving source, tracing the walls of the cavity. Apparently, the HH 83 system could mimic the HHL 73 scenario.

However there are significant differences between both objects. First, the bulk of the HHL 73 emission detected is line emission, with small, if any, continuum contribution. In contrast, the emission from the bow-shaped base of the HH 83 jet has an appreciable continuum contribution. Second, the radial velocities measured in HHL 73 present both redshifted and blueshifted values, while the radial velocities along the HH 83 jet are only blueshifted. Thus, a different scenario with another geometry than that proposed for the HH 83 system should be assumed to explain the spatial distribution of the HHL 73 velocities. In addition, the separation between *IRAS* 21432+4719 and the optical and near-*IR* emission of HHL 73 is appreciably larger than that between *IRAS* 05311–0631 and the base of the HH 83 jet (~ 13 arcsec or ~ 0.03 pc for a distance of 460 pc). However, as already discussed, *IRAS* 21432+4719 could be located closer to the apex of HHL 73 than the position given by the *IRAS* Point Source Catalogue.

Let us describe a qualitative scenario compatible with the complex HHL 73 kinematics derived from IFS data. Let us assume that the YSO exciting HHL 73 is deeply embedded and located to the northeast of HHL 73, near the apex of the HHL 73 emission. This source is ejecting supersonic gas with a low-collimation pattern (as, e. g., from a disc- or X-wind) and, in addition, is driving a highly-collimated outflow (see, for example, Takami et al. (2006) and references therein, where several models giving rise to outflows having low- and high- velocity components are discussed). The low-collimated gas flowing outside the dark cloud can give, by projection effects, both the low-blueshifted and the redshifted observed velocities (i. e. the main contributors to the BLVC and RVC), while the BHVC would mainly arise from the high-collimated outflow. The global kinematic pattern obtained from such a scenario would then mimic that produced by an outflow having a redshifted and two (low and high) blueshifted velocity components, even if all the supersonic gas we are observing is actually flowing outside the dark cloud (see the sketch in Fig. 17).

5 CONCLUSIONS

From the analysis carried out of the CCD and IFS HHL 73 observations, complemented with those available from the literature we found:

The bulk of the HHL 73 optical red emission is mainly line emission from shock-excited gas, such as is usually found in HH objects. Continuum emission from dust scattered starlight, if present, seems to be weak.

High-spatial resolution, narrow-band images of HHL 73 resolved its bow-shaped morphology into two components and a collimated emission ~ 4 arcsec long emerging towards the west, which is reminiscent of a microjet.

The kinematics of HHL 73 derived from the IFS data show that the emission is supersonic, with both blueshifted and redshifted velocities. From a line-profile multicomponent model, we were able to resolve three velocity components for the [S II] $\lambda\lambda 6717, 6731$ Å emission lines. These kinematic components correlate with the morphological components discovered from the high-resolution CCD images. The redshifted component, being the most extended one, spatially correlates with the bright, extended HHL 73 emission, elongated in the north–south direction. Its spatial distribution is also in good agreement with that of the radio continuum emission. The two blueshifted (low- and high-velocity) components are morphologically well correlated with the northwestern HHL 73 emission and the microjet. In order to mimic the complex kinematic pattern derived from the IFS spectra, we tentatively propose a scenario involving both low- and highly-collimated supersonic gas ejected from a YSO.

In the light of the data here discussed, we propose that the exciting source of HHL 73 (and possibly of HH 379) is deeply embedded in the dark cloud causing the high extinction, lying to the northeast of HHL 73, close to its apex. In spite of its angular separation, *IRAS* 21432+4719 is the most plausible candidate to be tracing the low-/intermediate YSO that is driving the centimetre, *IR* and optical emission associated with HHL 73, although high sensitivity observations with high angular resolution in the millimetre wavelength range, not affected by extinction, are needed to confirm this issue and to establish clearly the location and properties of the HHL 73 driving source.

Further observations, both in the centimetre wavelength range and IFS data covering the wavelength range blueward of $H\alpha$, to include high-excitation HH emission lines, are needed to settle the nature of the HHL 73 object completely.

ACKNOWLEDGMENTS

We acknowledge the Support Astronomer Team of the IAC for obtaining the NOT images. We thank Aina Palau for help with the MSX data. We appreciate Terry Mahoney's help with the manuscript. The authors were supported by the Spanish MEC grants AYA2005-08523-C03-01 (RE, RL, AR and GB), AYA2005-09413-C02-02 (SFS), AYA2006-13682 (BGL) and AYA2005-08013-C03-01 (AR). In addition we acknowledge FEDER funds (RE, RL, AR and GB), and the Plan Andaluz de Investigación de Junta de Andalucía as research group FQM322 (SFS). ALFOSC is owned by the Instituto de Astrofísica de Andalucía (IAA) and operated at the NOT under agreement between IAA and the NBIfAFG of the Astronomical Observatory of Copenhagen. This publication makes use of data products from the Two Micron All Sky Survey, which is a joint project of the University of Massachusetts and

the Infrared Processing and Analysis Center/California Institute of Technology, funded by the National Aeronautics and Space Administration and the National Science Foundation, and data products from the Midcourse Space Experiment (MSX). We thanks the anonymous referee for his/her useful information and comments.

REFERENCES

- Anglada G., 1995, *Rev. Mex. Astron. Astrof. C. S.*, 1, 67
 Anglada G., Rodríguez L. F., Cantó J., Estalella R., Torrelles J. M., 1992, *ApJ*, 395, 494
 Anglada G., Sepúlveda I., Gómez J.L., 1997, *A&ASS*, 121, 255
 Bacciotti F., Mundt R., Ray T.P., Eislöffel J., Solf J., Camezind M., 2000, *ApJL*, 537, L49
 Beichman C.A., Myers P.C., Emerson J.P., Harris H., Mathieu R., Benson J.P., Jennings R.E., 1986, *ApJ*, 307, 337
 Cantó J., 1981, *Investigating the Universe*, ed. F. Kahn, Dordrecht, Reidel, p. 95
 Connelley M.S., Reipurth B., Tokunaga A.T., 2007, *AJ*, 133, 1528
 Davis C.J., Ray T.P., Desroches L., Aspin, C., 2001, *MNRAS*, 326, 524
 Davis C.J., Whelan E., Ray T.P., Chrysostomou, A., 2003, *A&A* 326, 524
 Devine D., Reipurth B., Bally, J., 1997, Low-mass star formation-from infall to outflow, poster Proc., F. Malbet, & A. Castets, IAU Symp., 182, 91
 Dobashi K., Onishi T., Iwata T., Nagahama T., Patel N., Snell R.L., Fukui Y., 1993, *AJ*, 105, 1487
 Dobashi K., Yonekura Y., Mizuno A., Fukui Y., 1993, *AJ*, 104, 1525
 Elias J.H., 1978, *ApJ*, 233, 859
 Garay G., Brooks K. J., Mardones D., Norris R. P., 2003, *ApJ*, 587, 739
 García-Lorenzo B., Acosta-Pulido J., Megias-Fernández E., 2002, in *ASP Conf. Ser. 282, Galaxies: The Third Dimension*, ed. M. Rosado, L. Binette, & L. Arias (San Francisco: ASP), 501
 Gyulbudaghian A.L. 1984, *Astrofizika*, 20, 631
 Gyulbudaghian A.L., Rodríguez L.F., Mendoza-Torres E. 1987, *Rev. Mex. Astron. Astrof.*, 15, 53
 Harris S., Clegg P., Hughes J., *MNRAS*, 1988, 235, 441
 Kelz A., Verheijen M.A.W., Roth M.M. et al., 2006, *PASP*, 118, 129
 Kewley L.J., Dopita M.A. 2002, *ApJS*, 142, 35
 Lavalley-Fouquet C., Cabrit S., Dougados C., 2000, *A&A*, 356, L41
 López, R., Raga, A.C., Riera, A., Anglada, G., Estalella, R. 1995, *MNRAS*, 274, L19
 Martí J., Rodríguez L. F., Reipurth B., 1993, *ApJ*, 416, 208
 Ojha D.K., Tamura M., Nakajima Y., Fukagawa M., 2004, *ApJ*, 608, 797
 Palla F, Stahler S.W., 1993, *ApJ*, 418, 414
 Pravdo S. H., Rodríguez L. F., Curiel S., Cantó J., Torrelles J. M., Becker, R. H., Sellgren K., 1985, *ApJ*, 293, L35
 Reipurth B., 1989, *A&A*, 220, 249
 Rodríguez L. F., Garay G., Brooks K. J., Mardones D., 2005, *ApJ*, 626, 953
 Rodríguez L. F., Ho P. T. P., Torrelles J. M., Curiel S., Cantó J., 1990, *ApJ*, 352, 645
 Rodríguez L. F., Reipurth B., 1989, *Rev. Mex. Astron. Astrof.*, 17, 59
 Roth M. M., Kelz A., Fechner T., Hahn T., Bauer S.-M., Becker

- T., Böhm P., Christensen L., Dionies F., Paschke J., Popow E.,
Wolter D., Schmoll J., Laux U., Altmann W., 2005, PASP, 117,
620
- Sánchez, S. F. 2004, AN, 325, 167
- Sánchez S. F. 2006, AN, 327, 850
- Siess L., Dufour E., Forestini M., 2000, A&A, 358, 593.
- Smith M.D., 1995, A&A, 296, 789
- Takami M., Chrysostomou S., Ray T.P., Davis C.J., Dent W.R.F.,
Bailey M., Tamura M., Terada H., Pyo T.S., 2006, ApJ, 641, 357

This paper has been typeset from a \TeX / \LaTeX file prepared by the author.